Discover Materials

Discover

Research

Facile fabrication of triboelectric nanogenerators based on paper and natural rubber as low-cost bio-derived materials

K. Paige Williams[1] · Noah Hann-Deschaine[1] · Div Chamria[1] · Hans T. Benze[1] · Ramesh Y. Adhikari[1]

Received: 31 October 2022 / Accepted: 17 January 2023
Published online: 21 January 2023

Abstract
Triboelectric nanogenerators (TENGs) are devices capable of effectively harvesting electrical energy from mechanical motion prevalent around us. With the goal of developing TENGs with a small environmental footprint, herein we present the potential of using rubber and paper as biological materials for constructing triboelectric nanogenerators. We explored the performance of these TENGs with various contact material combinations, electrode sizes, and operational frequencies. The optimally configured TENG achieved a maximum open circuit output voltage of over 30 V, and a short circuit current of around 3 μA. Additionally, this optimally configured TENG was capable of charging various capacitors and achieved a maximum power output density of 21 mW/m^2. This work demonstrates that biologically derived materials can be used as effective, sustainable, and low-cost contact materials for the development of triboelectric nanogenerators with minimal environmental footprint.

1 Introduction

The need for renewable and clean energy sources has become increasingly urgent in modern society. Unsustainable consumption of energy resources, the exponentially increasing ecological problem of electronic waste (e-waste), and the ever-accelerating demand for electronic devices make the search for a viable alternative more critical than ever [1, 2]. One way to address these issues is to develop a mechanism to harvest untapped residual energy such as vibrations and mechanical motions created while operating machines, blowing wind, moving water, or during biological motion. Another potential solution is to develop electronic components that are naturally sourced and biodegradable and therefore leave the smallest possible environmental footprint. Therefore, the electronic components derived from biological materials and capable of generating power from mechanical motion would serve to minimize environmental impact as well as harvest energy from residual mechanical motions prevalent all around.

Triboelectric nanogenerators (TENGs), known for converting mechanical energy into electricity by coupling contact electrification and electrostatic induction, are receiving attention due to their simple design, range of materials that can be utilized, high efficiency, low cost, reliability, and robustness [3, 4]. As the interest and need to develop "green electronics" continue to grow to help address the problems of e-waste [5, 6], various studies on the development of TENGs based on natural materials have been carried out [7, 8]. Materials derived from animals such as chitin, silk fibroin,

Supplementary Information The online version contains supplementary material available at https://doi.org/10.1007/s43939-023-00036-8.

✉ Ramesh Y. Adhikari, radhikari@colgate.edu | [1]Department of Physics & Astronomy, Colgate University, 13 Oak Drive, Hamilton, NY 13346, USA.

and egg white [9], spider silk protein [10], silk-worm silk [11], and gelatin [12] have been used as dielectric materials for TENGs. Parts from plants such as leaves [13, 14] and petals [15] have also been used as bio-derived dielectric materials for TENGs. Processed plant materials such as cellulose [16] have also been used for constructing TENGs either as cellulose paper [17] or as composite by mixing with other polymers such as polydimethylsiloxane (PDMS) [18] or 2D materials such as phosphorene [19]. However, a majority of these TENGs constitute complementary contact dielectric materials that are not of biological origin. Materials such as polydimethylsiloxane (PDMS), polytetrafluoroethylene (PTFE), polyvinyl chloride (PVC), and polyimide (PI) sheets are routinely used as complementary dielectric materials for making surface contact during TENG operation. This has been true for various paper-based TENGs that have been reported as well [7, 8, 20]. For instance, among various paper-based TENGs that have been developed, PI sheet [21], PDMS [22], and Teflon [23] have been used as complementary dielectric materials. There have also been reports of various configurations of TENGs based on rubber as another bio-derived material. However, those devices have either been based on single electrode architecture [24] or, in the case of TENGs that undergo contact-separation during operation, rubber has been used as a composite with materials such as PTFE [25], TiO_2 [26], and Ag [27] and/or with an inorganic dielectric such as PDMS [25, 28, 29], Teflon [27], and PTFE [26] as the complementary contact layer.

Here, we report the construction of TENGs that operate in vertical contact-separation mode (VCSM) and comprise both contact dielectrics of biological origin, namely, paper and natural rubber. Furthermore, we compare the performance of these rubber-based TENGs (R-TENGs) with the TENGs with polyimide (PI/Kapton) films which have been used in various other TENGs [21, 30, 31]. We optimized the performance of the R-TENGs by investigating their performance at various operational frequencies, material combinations, and electrode sizes. We studied the performance of R-TENGs based on two different kinds of rubber sheets with different thicknesses and surface textures as one of the dielectric materials. For the second dielectric material, we chose paper for various reasons. Paper not only consists of micro and nanofibers which can improve the electrical output by improving frictional contact, but is also a widely available, low-cost, sustainable, and eco-friendly material. Additionally, although paper is known to possess poor triboelectric properties in comparison to other materials, it has been shown that its potential as a reliable dielectric material for TENG is greatly enhanced when chemically modified [21]. To enhance the triboelectric properties of the paper, we introduced a low concentration of polyvinylidene fluoride (PVDF) solution onto the paper surface to improve its ability to gain electrons without compromising the surface roughness.

We found that the optimal R-TENG consisted of a material combination of the thick rubber sheet as one dielectric material and PVDF-coated paper as the second dielectric material operating at a contact frequency of 2 Hz. The maximum open circuit voltage and short-circuit current of our optimized R-TENG reached over 30 V and 3 μA, respectively. Additionally, it achieved a maximum output power density of around 21 mW/m^2 when the external load resistance of 1 GΩ was used. Finally, we found that the optimized R-TENG was capable of powering various sizes of capacitors, including charging a $10\mu F$ capacitor to around $2.6V$ in less than 2 min.

2 Materials and methods

2.1 Materials

Natural gum thick rubber sheet (thickness 0.0625 in, Mfr. Model # BULK-RS-NAT40-23) and polyimide (PI) sheet (thickness 0.001 in, Mfr. Part ID: BULK-PF-PI-1) were purchased from Grainger, Inc. Natural thin rubber sheet (thickness 0.008 in, Part # 85995K13) was purchased from McMaster-Carr. Poly(vinylidene fluoride) (PVDF) powder (182702-5G) was bought from Millipore Sigma. Staples brand commercial printer paper was purchased from Staples Inc.

2.2 Fabrication of PVDF paper

All the materials described above, except the printer paper, were used as is without any chemical modification of the surface. The printer paper was treated with a PVDF solution following a procedure described elsewhere [21]. The process is as follows. We first prepared 1% weight concentration of PVDF solution by mixing 0.2 mg of PDVF with 20 mg (25.5 mL) of acetone as solvent. A cut piece of printer paper was then placed onto a hot plate at 70 ℃. The PVDF-treated paper, which is also called PVDF-paper in this report, was prepared by squirting 2–3 mL of PVDF solution from a syringe on the paper. The solvent fully evaporated in 5 min leaving a dry PVDF-coated paper.

2.3 Linear actuator station

A stepper motor driven linear actuator provided consistent and periodic contact between the dielectric during the operation of TENGs. A 300 mm travel length Linear Actuator Stage with NEMA17 Stepper Motor (SainSmart, Part# 249703801) was used. The motor was driven by SainSmart TB6600 CNC Micro-Stepping Motor Driver which was powered by a LETOUR 36 V power supply with EMC Filter. A Teensy 3.2 microcontroller was programmed with the program available in the AccelStepper Arduino library to control the speed and acceleration of the linear actuator. The microcontroller program also received variable analog inputs to adjust the travel distance, speed, and acceleration. These three variables could be changed to adjust the frequency of the linear actuator.

2.4 Electrical characterization

All the current and voltage measurements were carried out with Keithley DMM6500 Multimeter.

2.5 AFM imaging

AFM topography imaging was used to characterize the surface profile of all the materials used as dielectric layers in the TENGs. The AFM topography imaging was carried out with Bruker ICON AFM in ScanAsyst-Air Mode with the help of the SCANASYST-AIR probe. Kelvin Probe Force Microscopy (KPFM) was carried out with the SCM-PIT V2 probe in AM-KPFM mode. The interleave mode was used with an applied potential of 0.5 V.

2.6 FTIR spectroscopy

Attenuated total reflection (ATR) FTIR spectroscopy was carried out with Nicolet 6700 FTIR spectrometer. The scan resolution was 2 cm^{-1} with 64 scans within a scan range of 650 cm^{-1} to 4000 cm^{-1}.

3 Results and discussion

3.1 Design of R-TENGs

A TENG is a device with at least one electrode, usually coated on a dielectric layer, which undergoes periodic contact and separation with another dielectric material. TENGs can operate in four different working modes: vertical contact-separation mode (VCSM), lateral sliding mode (LSM), single electrode mode, and freestanding triboelectric layer mode [8]. The R-TENGs in our research were investigated in VCSM, according to which two dielectric materials, each connected to electrodes, are repeatedly brought in contact and then pulled apart during operation. VCSM is the most common of the four working modes due to its simple structural design and working method [8]. The TENG that we studied had four layers as shown in the sketch (Fig. 1a). The top dielectric layer consisted of a rubber sheet on which copper tape was applied to act as an electrode. The bottom dielectric was either PVDF-paper or PI film on which copper tape was applied to act as the bottom electrode. We used a homemade linear actuator to drive R-TENGs with constant contact force on all measurements. The entire electrode-dielectric surface was covered with PI material for insulation and secured with Kapton tape. All the measurements were carried out at room temperature and humidity.

3.2 Operating principle of R-TENG

TENGs exploit a process called triboelectrification, also known as contact electrification, where usually two dissimilar dielectric materials are brought into momentary frictional contact resulting in the transfer of the charges across the surface interface of dielectric materials making those surfaces electrically charged [3, 32]. This transfer of charges results in an excess of electrons on the surface of one material and a deficit on the surface of the other, thereby, creating an electric potential difference. To maintain electroneutrality, opposite charges are then electrostatically induced into the attached electrode during which current flows through the circuit. This repeated cycle of contact and separation of dielectric materials drives current to flow cyclically in both the positive and negative direction, thereby generating a continuous AC output. As stated above, R-TENGs used in this research were operated in VCSM mode (Fig. 1b–e). The

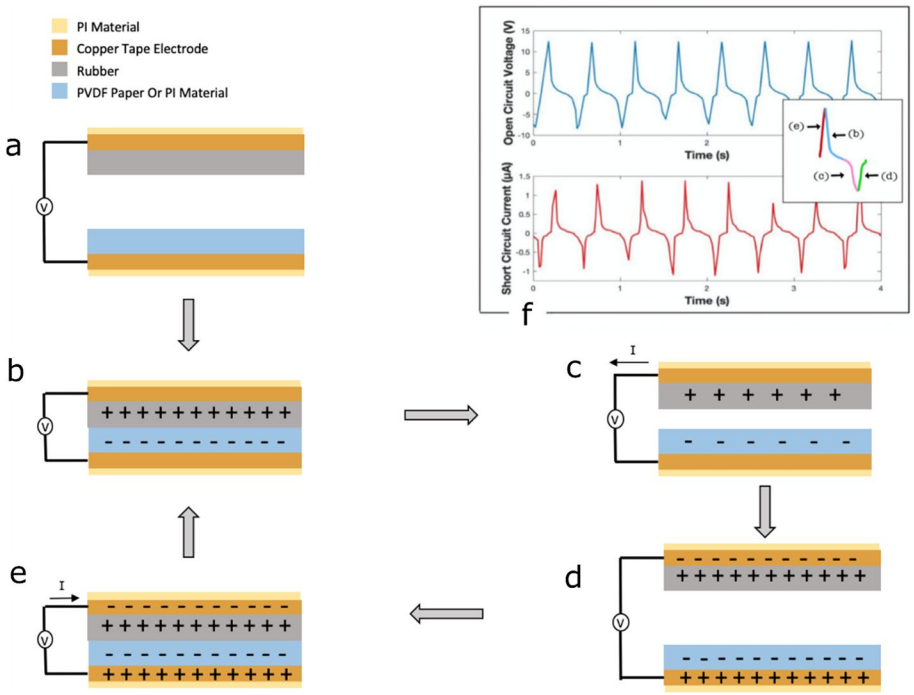

Fig. 1 **a** Schematic of the R-TENG. **b**–**e** Schematic representation of the operation mechanism of the R-TENG in VCSM. **f** Example of the typical electrical output characteristics of the R-TENG in terms of both open circuit voltage and short circuit current, along with a magnified inset of a single VCSM cycle

positive terminal of a multimeter was connected to the electrode attached to the bottom dielectrics (PVDF-paper or PI sheet), while the negative terminal was connected to the electrode attached to the top dielectrics (thin or thick rubber sheet). Prior to contact, the two materials are uncharged and no current flows (Fig. 1a). However, due to triboelectrification, contact electrification occurs on the material surfaces once they come into contact due to an external mechanical force (Fig. 1b). Since the surface electron affinity of PI film or PVDF-paper, used as bottom dielectric, is higher than that of the rubber, used as top dielectric, electrons are transferred from the surface of the top dielectric to the surface of the bottom dielectric. Thus, positive charges are generated on the surface of the top dielectric and negative charges on the surface of the bottom of the dielectric which was verified with a multimeter. The exact mechanism of transfer of charge across surfaces upon contact between two materials is not exactly clear. While the conventional thought has been that electron transfer occurs during contact between dielectric material [20], there have been recent reports suggesting that, especially when dealing with polymeric materials such as natural rubber used in this study, the charge transfer could involve covalent bond-break and material transfer [33, 34]. Nevertheless, despite the charge transfer across the surface after contact, the current does not flow through the external load since the electrostatic equilibrium is maintained at the contact surface of the top and bottom dielectrics (Fig. 1b).

However, upon the separation of surfaces in contact, this electrostatic equilibrium is broken. An electrical potential difference is thereby created between the dielectrics and the electrodes attached to them. This induces the movement of electrons between the electrodes through the external load generating current through the circuit (Fig. 1c). When the charges in the electrodes and the dielectric materials reach equilibrium once again, current ceases to flow through the external load (Fig. 1d). As the contact occurs again, current flows in the opposite direction as the surfaces in contact achieve electrostatic equilibrium and the induced charges on the electrodes from the previous step neutralize each other (Fig. 1e). Finally, the process repeats itself through the steps schematically shown in Fig. 1b–e as the materials repeatedly come into contact and then separate during operation of the TENG.

A typical electric output characteristic involves current and voltage peaks when the dielectric surfaces come in contact as well as when they separate (Fig. 1f). The magnified inset helps to further explain the VCSM cycle. When the dielectric surfaces come in contact during the cycle, there is a sudden increase in the current through the load as the excess charges on the electrodes are neutralized. After the contact, the current suddenly diminishes as the electrode neutralization has completed and charges on top and bottom dielectrics are in electrostatic equilibrium. When the dielectric layers are again separated, electrostatic equilibrium is broken and due to the electric fields from the charged dielectric surfaces, opposing charges on the attached electrodes are induced. During this process, a sudden current is generated until the induced charges on the electrodes reach electrostatic equilibrium with the attached charges dielectrics. Soon after the

equilibrium is achieved, the current diminishes again until the dielectric surfaces are brought in contact again breaking the electrostatic equilibrium between the electrodes and the dielectrics attached to them.

The generation of surface charge during the operation of VCSM TENGs creates an electric field across the surfaces that come into contact as those surfaces separate. The electric field due to a charged layer of length (L) and width (W) with a uniform surface charge density (σ) in a medium with certain permittivity (ϵ) is given as [3, 35, 36]:

$$E_z = \frac{\sigma}{\pi\epsilon} arctan\left[\frac{L/W}{2(z/W)\sqrt{4(z/W))^2 + (L/W)^2 + 1}}\right] = \frac{\sigma}{\pi\epsilon} f(z) \tag{1}$$

where, z is the distance from the charged surface. Therefore, the electric field strength varies as the distance between the contact surfaces changes during mechanical motion. Since the electrodes are placed on the other side of the top and the bottom dielectrics with thicknesses a and b respectively, the potential difference between the electrodes which is responsible for driving the current through the external load and the value that can be recorded by the multimeter would be:

$$\Delta V = V_a - V_b = -\int \overrightarrow{E_a} \cdot \overrightarrow{dl} + \int \overrightarrow{E_b} \cdot \overrightarrow{dl} = -\frac{\sigma}{\pi\epsilon_a}\int_a^{a+z} f(z)dz + \frac{\sigma}{\pi\epsilon_b}\int_b^{b+z} f(z)dz \tag{2}$$

The short circuit output current (I_{SC}) for the device is then given as:

$$I_{SC}(t) = LW\frac{d\sigma(t)}{dt} \tag{3}$$

The total amount of charge generated on the electrode surface during the contact-separation cycles can then be calculated as:

$$Q_{SC} = LW\sigma = \int_{t_0}^{t} I_{SC}(t)dt \tag{4}$$

where $t - t_0$ would be the duration of operation of the device.

3.3 Optimization of R-TENG performance with the operational frequency and material combinations

To enhance the electrical performance of R-TENG, we investigated the amount of open circuit voltage (V_{OC}) and short circuit current (I_{SC}) generated for various operational frequencies and material combinations (Fig. 2). Low frequencies ranging from 0.5 to 2 Hz were used for this study. TENG performance at low frequencies is of significance because a lot of natural motions occur in the low-frequency range [13]. Regarding the dielectrics used for exploration, the top dielectric material was either a thick or thin natural rubber sheet while the bottom dielectric was either PVDF-paper or PI sheet. It is to be noted that the thick and thin rubber sheets were of different textures and elasticity. Thick rubber was less elastic with a manufacturer-specified tensile strength of 3,000 psi while the value for the tin rubber was 4,000 psi. Thick rubber, thin rubber, and paper were used for their natural origin and eco-friendliness. On the other hand, the PI film was used since it is commonly used as a dielectric material for TENGs and therefore, it would allow us to compare the performance between all-natural R-TENG consisting of rubber and paper vs. R-TENG with rubber and PI film.

All the R-TENGs constructed for this study had dielectric contact surface and electrode area of $7 \times 5cm^2$. We observed that both V_{OC} and I_{SC} increased for all R-TENGs as the frequency increased (Fig. 2a, b). These values for R-TENGs consisting of thin rubber sheet started to saturate towards 2 Hz while the values for R-TENGs consisting of thick rubber continued to increase with increasing frequency. This increase in performance of a TENG with increasing frequency has been suggested due to the increase in the rate of charge transfer as the speed of contact and separation cycle increases [35, 37]. Among four different combinations, the maximum V_{OC} and I_{SC} values were observed with the R-TENG with thick rubber as the top dielectric and PVDF-coated paper as the bottom dielectric with max-V_{OC} of about $33V$ (i.e. $\sim 66V_{Peak-Peak}$) and max-I_{SC} of about $3\mu A$.

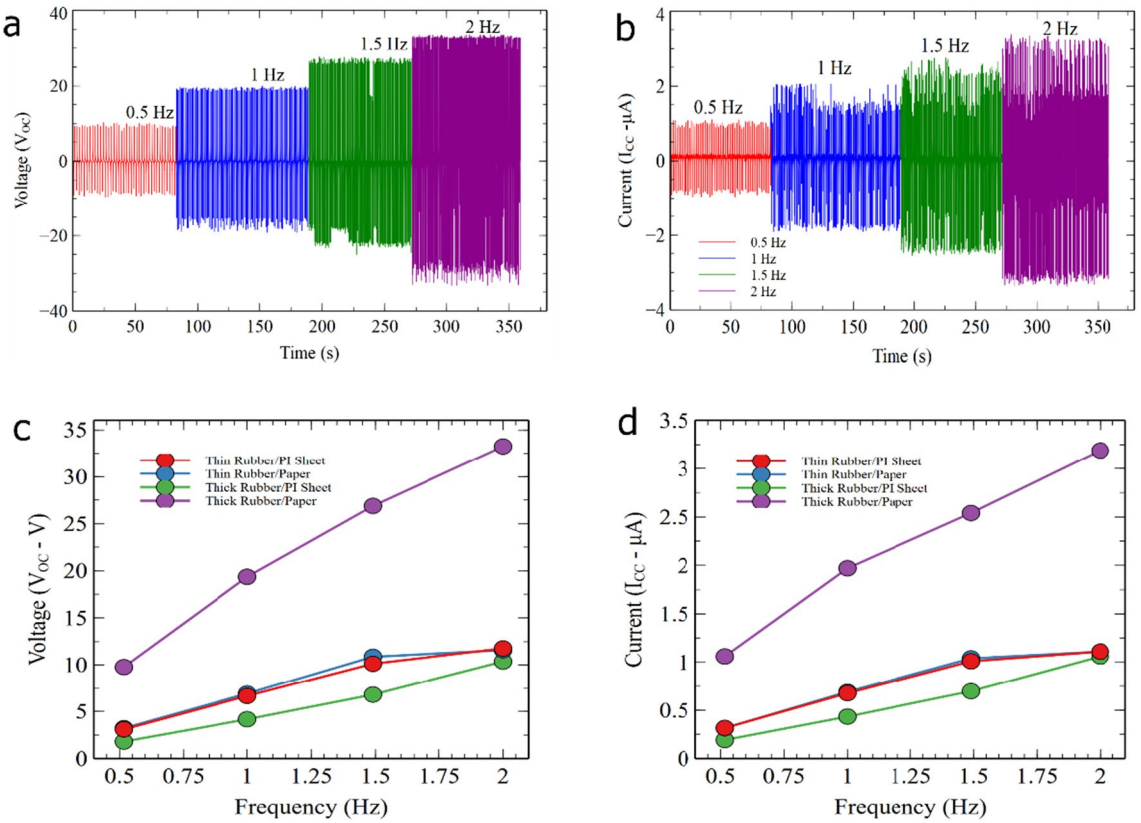

Fig. 2 **a** Open-circuit voltage (V_{OC}) and **b** short circuit current (I_{SC}) during operation of R-TENG with thick rubber and PVDF-coated paper as contact surfaces at different frequencies. **c** V_{OC} and **d** I_{SC} for various R-TENGs as a function of operational frequencies

Various parameters associated with contact dielectric materials such as surface roughness [38, 39], surface functional groups [40, 41], and hardness of the elastomer material [39] can affect the performance of a TENG. In order to understand the relationship between the surface roughness of the dielectric materials and the performance of the R-TENGs in this study, we carried out SEM and AFM studies on all four different dielectric materials (Fig. 3, Fig. S1). We observed that the thick rubber had circular microscale structures distributed all over the surface (Fig. 3a, e). Thin rubber surface had highly irregular surface morphology (Fig. 3b, f). However, these features were smaller in their height compared to regular shaped microstructures for thick rubber. Therefore, the roughness parameters for the thick rubber surfaces were about two times higher than for the thin rubber surface. According to the manufacturer's specification, both of the rubber sheets used in this study had the same durometer value of 40A indicating the same level of hardness of these elastomers and hence the same extent of the cohesive energy of the materials. It has been suggested that given the same hardness level, the roughness of materials significantly enhances charge generation on the surface after contact[39]. In addition, the ATR-FTIR spectroscopy (Fig. S2) of the thick rubber sheet surface demonstrated strong peaks at 1537 cm^{-1} which is associated with C–H stretching and N–H in-plane bending, at 2847 cm^{-1} which is associated with $-CH_2$ stretching, and at 2915 cm^{-1} which is associated with $-CH_3$ stretching[42]. While on the other hand, the thin rubber surface has a strong peak at 1010 cm^{-1} which is associated with C–C stretching[42]. KPFM imaging of the surfaces (Fig. S3) demonstrated that the thick rubber surface generates more charge than the thin rubber surface. Therefore, the abundance of N–H and –C–H groups at the surface coupled with a higher level of surface roughness makes it possible for a thick rubber sheet to generate more surface charges and therefore improve the performance of the R-TENG compared to using a thin rubber sheet.

Regarding the bottom dielectric, the PVDF-paper surface had nano to microscale features (Fig. 3c, g) which were absent in PI film (Fig. 3d, h), also evident from the roughness analysis from AFM images. Furthermore, the FTIR analysis of the pristine paper and PVDF-paper (Fig. S4) demonstrated that the α-phase crystallization of PVDF was prevalent on the PVDF-paper surface (Fig. S5) which is the most commonly occurring phase [43]. This phase is not as electroactive as β-phase crystalline PVDF [44], but given the abundance of –C–H and N–H functional groups on the thick rubber surface, it is reasonable that the –F functional groups on PVDF-paper surface can act as electron affinity sites. Therefore, the

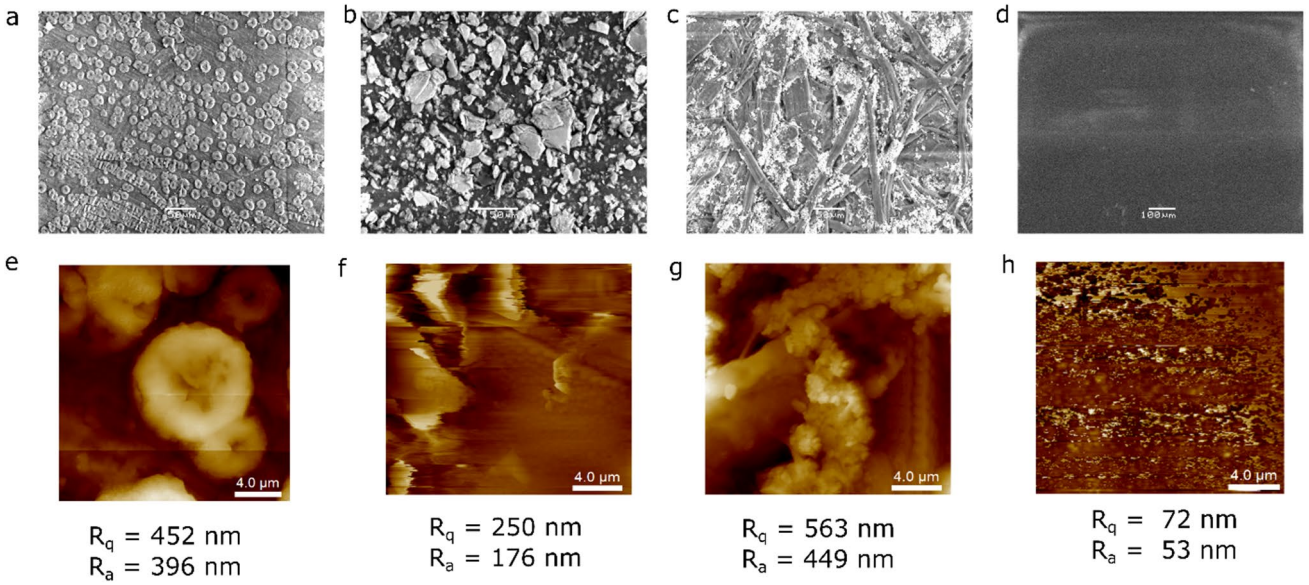

Fig. 3 Surface morphology of dielectric surfaces used in R-TENG. SEM images of surfaces of **a** thick rubber sheet, **b** thin rubber sheet, **c** PVDF-paper, and **d** PI film. Scale bars are 50 µm except for PI film which is 100 µm. AFM images of **e** thick rubber sheet, **f** thin rubber sheet, **g** PVDF paper, and **h** PI film. Scale bars are 4 µm. Corresponding roughness parameters extracted from the AFM images are listed underneath the AFM images

roughness of the surface coupled with the abundance of -F functional group made PVDF-paper surface perform much better than the PI film. KPFM images of the dielectric surfaces also demonstrated higher surface charge for PVDF-paper than for PI film (Fig. S3). Therefore, it is understandable that the R-TENG with the combination of thick rubber sheet and PVDF-paper had the highest electrical performance.

3.4 Optimization of R-TENG performance with electrode size

In TENGs operated in VCSM, the general practice has been to use both electrodes with the same area. However, in various other modes of TENGs, it has been suggested that the area and geometries of the electrodes could play role in the electrical performance of TENGs due to the edge effect playing a role [21, 45–49]. There have been reports of studies performed on VCSM TENGs with the size of both of the electrodes increased, keeping parallel plate geometry intact during the process which resulted in the increase of V_{OC} and I_{SC} values with increasing electrode size [17]. However, in our study, we decided to keep the area of the bottom electrode to be the same as the area of the dielectrics but gradually increased the size of the top electrode as we recorded V_{OC} and I_{SC} values to study if the edge effect which have reported to have enhanced performance of the TENGs in other modes could also plays role in VCSM.

We kept the area of the bottom electrodes constant at $35cm^2$ with the dimension of $7cm \times 5cm$. While keeping the width of the top electrode constant at $5cm$, we increased the length from $0.5cm$ to $7cm$ resulting in electrode areas from $2.5cm^2$ to $35cm^2$. We observed an initial increase in both V_{OC} and I_{SC} as we increased the electrode area before both the values started levelling off (Fig. 4a, b). This suggests that simply increasing the electrode area does not necessarily provide the best performance of the TENG and there is an optimal area that maximizes the outputs such as V_{OC} and I_{SC}.

The value of V_{OC} during a TENG operation is given as [46, 49]:

$$V_{OC} = \frac{Q_{SC}}{C} \tag{5}$$

where, Q_{SC} is charge transferred during the short circuit as defined in Eq. (4) and the C is the capacitance between the two electrodes of the TENG. Considering the edge effect in a non-ideal parallel electrode capacitor that is formed in a TENG due to one charged surface being smaller than the other, it has been demonstrated that V_{OC} can be related to the electrode dimensions as [49]:

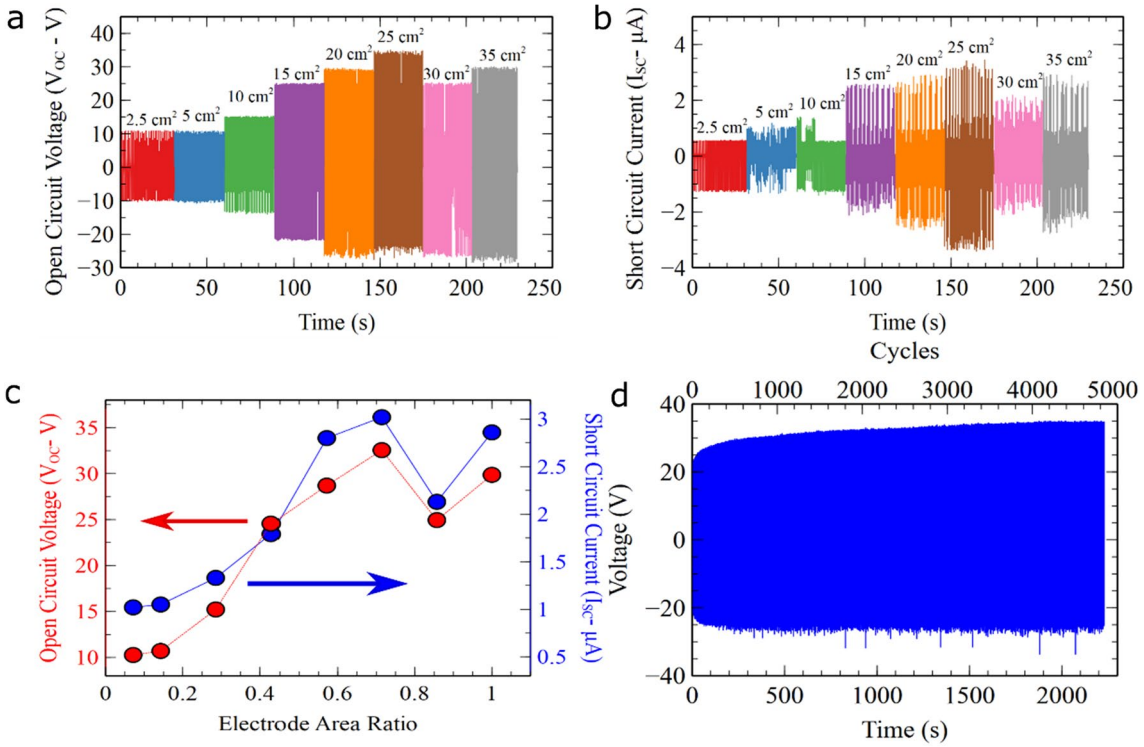

Fig. 4 **a** V_{oc} and **b** I_{sc} output profile for thick rubber-PVDF paper R-TENG as the area of one of the electrodes is increased while keeping another electrode area constant. **c** Average of maximum V_{OC} (red) and I_{SC} (blue) as the function of the ratio of electrode areas. **d** V_{OC} output of Thick Rubber and PVDF Paper R-TENG for about 4800 cycles of operation

$$V_{OC} = \frac{\sigma}{2\epsilon_0}\pi L \tag{6}$$

for smaller L. However, as the size of the electrode is increased, the parallel plate geometry starts to become more ideal while the edge effect diminishes resulting in the expression:

$$V_{OC} = \frac{\sigma g x ln(L)}{\pi \epsilon_0 L} \tag{7}$$

for large values of L, where g is the gap between the electrodes , x is the separation of the dielectrics in a TENG. Equation 6 suggests that V_{OC} should rise with an increase in the electrode length, just as we observe in our R-TENG. Equation 7 suggests that for a larger electrode, V_{OC} should start to diminish, as we observed in our experiment. In our case, since one of the electrodes had a constant large area of $35cm^2$ while the area of the second electrode was increased, we noticed that the maximum V_{OC} and I_{OC} was achieved when the ratio between the smaller and the larger electrode was 0.7 (Fig. 4c). Below this ratio, the performance of the R-TENG continuously improved while when the electrode ratio went over 0.7, the performance of the R-TENG diminished.

Since the operation of the TENGs involves mechanical motion with constant frictional contact between the dielectric surfaces, one of the important features of a reliable TENG would be its ability to perform over a long period without undergoing wear and tear. When we operated the R-TENGs that we developed, we did not observe any degradation in the performance of TENG during their operation for thousands of cycles (Fig. 4d). This demonstrates that R-TENGs derived from biological materials can operate reliably over a long period.

3.5 Optimization of R-TENG performance with external load

Finally, we evaluated the power output of the previously optimized R-TENG with the thick rubber as the top dielectric and PDVF-coated paper as the bottom dielectric, with $5cm \times 5cm$ electrode attached to the paper and $5cm \times 7cm$ electrode attached to the thick rubber while operating at $2Hz$ frequency. We used external load resistances ranging from 1kΩ to 1GΩ and observed that the voltage output increased almost steadily as the load resistance was increased, while the current initially decreased and then gradually increased (Fig. 5a). Using the value of current through load resistors at corresponding voltage outputs, we calculated the power output of R-TENG (Fig. 5b). We observed that the power output of the R-TENG depended on the load resistance as expected. The power density significantly increased once we used the load resistance with values higher than $1M\Omega$. As we increased the load resistance to $1G\Omega$, it appeared that we were approaching the maximum peak power density, indicative of high internal resistance in the R-TENG as the maximum power output is achieved when the load resistance is similar in value to the internal resistance of a TENG [21, 35]. With the internal resistance of the multimeter being $10M\Omega$ and from the fact that it was connected in parallel with the load resistor of $1G\Omega$ (Fig. S6), the equivalent resistance in the circuit due to the load and multimeter would be $9.9M\Omega$. Therefore, the internal resistance of the TENG was at around $10M\Omega$. At the load resistance of $1G\Omega$, the power density of the R-TENG was about $21mW/m^2$ (i.e. $2.1\mu W/cm^2$). This power density is similar to the TENG based on rose petal-PMMA [15] and silk fibroin-rice paper [9] but slightly higher than TENGs based on cellulose nanofibril-phosphorene hybrid paper [19], and about five times higher than the TENG based on silk fibroin-PI film [11].

We also explored the possibility of storing the electrical energy generated by R-TENG in a capacitor (Fig. 5c). The R-TENG successfully charged commercial capacitors with the capacitance of $1\mu F$, $4.7\mu F$, and $10\mu F$. Since the TENG generated alternating current/voltage, we used a full wave bridge rectifier so that we could store charges in the capacitors. The $1\mu F$ capacitor reached a voltage of up to $3.6V$ in about 60 s, the $4.7\mu F$ capacitor charged to $3.4V$ in around $150s$, and finally, the voltage of the $10\mu F$ capacitors reached to around $2.6V$ in $150s$ (Fig. 5d). This demonstrates that the R-TENGs made almost entirely of plant-based materials such as natural rubber and paper can be used to convert mechanical energy to electrical energy that can be stored and possibly used for low power applications.

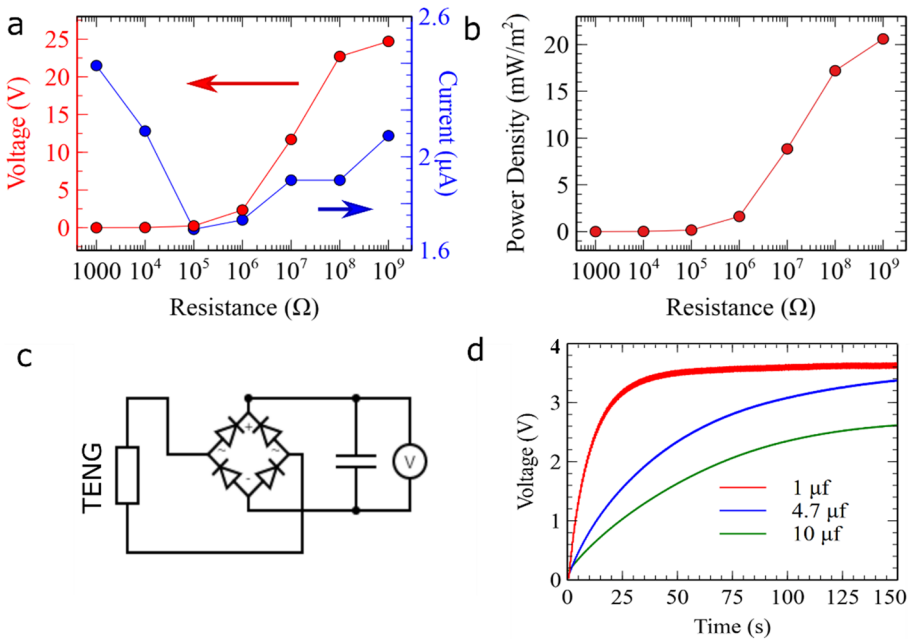

Fig. 5 **a** PVDF-paper and Thick Rubber TENG voltage (red) and current (blue) as a function of load resistance. **b** PVDF paper and Thick rubber TENG output power density as a function of load resistance. **c** Circuit diagram used to construct the circuit to charge capacitors. **d** Charging capacitors of various capacitance by operating optimized thick rubber and PVDF-paper R-TENG

4 Conclusion

In summary, we have developed rubber-based triboelectric nanogenerators (R-TENG) by using low-cost and readily available natural rubber sheets and paper. We explored the effects of operational frequencies, material combinations, and electrode sizes on the output performance of these R-TENGs while operating in VCSM. We were able to enhance the electrical output significantly by optimizing these variables and found that the optimal parameters were an electrode area ratio of 0.7, and an operational frequency of $2Hz$ with a dielectric combination of thick rubber and PVDF-treated paper as contact surfaces. The optimally configured R-TENG achieved an open circuit voltage (V_{oc}) of $33V$, and a short-circuit current (I_{sc}) of around $3\mu A$. Additionally, the optimally configured R-TENG was capable of charging various-sized capacitors and achieved a maximum power density output of $21mW/m^2$ when the load resistance was $1G\Omega$. The work reported here demonstrates that one can use cost-effective biologically sourced materials for residual mechanical energy harvesting using TENGs, especially for low-power applications. The lower cost of the materials also makes it viable to scale up. Utilization of eco-friendly, low-cost, and naturally sourced materials for alternative power sources such as TENGs as reported here open up avenues for widespread adoption while limitings the problems of e-waste by maintaining a minimal ecological footprint.

Acknowledgements This work was supported by Colgate University through the startup fund, Colgate Summer Research Fellowship, and Faculty Research Council as well as by National Science Foundation (NSF) Award No. 2203157. We thank Eric Muller in the Department of Chemistry for technical assistance.

Author contributions RYA conceptualized and supervised the project. HTB. developed the homemade electronically controlled linear actuator setup. KPW and NHD carried out the electrical measurements. RYA acquired the SEM and AFM topography images. DC acquired KPFM images and ATR-FTIR spectra. KPW, NHD, and RYA carried out the analysis. KPW prepared the original draft. RYA prepared subsequent drafts after review and edits from all other authors. RYA acquired the funding for the project. All authors read and approved the final manscript.

Data availability Most of the data generated during and/or analyzed during this study are included in this published article and its supplementary information files. The remaining datasets generated during the study are available from the corresponding author upon reasonable request.

Declarations

Competing interests The authors declare no competing interests.

References

1. Ahmed SF. The global cost of electronic waste. The Atlantic. 2016. https://www.theatlantic.com/technology/archive/2016/09/the-global-cost-of-electronic-waste/502019/. Accessed 20 May 2020.
2. Electronic waste poses 'growing risk' to environment, human health, UN report warns. UN News. 2017. https://news.un.org/en/story/2017/12/639312-electronic-waste-poses-growing-risk-environment-human-health-un-report-warns. Accessed 25 May 2020.
3. Dharmasena RDIG, Silva SRP. Towards optimized triboelectric nanogenerators. Nano Energy. 2019;62:530–49. https://doi.org/10.1016/j.nanoen.2019.05.057.
4. Lin Z-H, Cheng G, Lee S, Pradel KC, Wang ZL. Harvesting water drop energy by a sequential contact-electrification and electrostatic-induction process. Adv Mater. 2014;26(27):4690–6. https://doi.org/10.1002/adma.201400373.
5. Irimia-Vladu M. 'Green' electronics: biodegradable and biocompatible materials and devices for sustainable future. Chem Soc Rev. 2014;43(2):588–610. https://doi.org/10.1039/C3CS60235D.
6. Irimia-Vladu M, Eric D, Głowacki G, Bauer S, Voss G, Sariciftci NS. Green and biodegradable electronics. Mater Today. 2012;15(7–8):340–6. https://doi.org/10.1016/S1369-7021(12)70139-6.

7. Slabov V, Kopyl S, Soares dos Santos MP, Kholkin AL. Natural and eco-friendly materials for triboelectric energy harvesting. Nano-Micro Lett. 2020;12(1):42. https://doi.org/10.1007/s40820-020-0373-y.
8. Chao S, Ouyang H, Jiang D, Fan Y, Li Z. Triboelectric nanogenerator based on degradable materials. EcoMat. 2020. https://doi.org/10.1002/eom2.12072.
9. Jiang W, et al. Fully bioabsorbable natural-materials-based triboelectric nanogenerators. Adv Mater. 2018;30(32):1801895. https://doi.org/10.1002/adma.201801895.
10. Zhang Y, Zhou Z, Sun L, Liu Z, Xia X, Tao TH. 'Genetically Engineered' biofunctional triboelectric nanogenerators using recombinant spider silk. Adv Mater. 2018;30(50):1805722. https://doi.org/10.1002/adma.201805722.
11. Kim H-J, et al. Silk nanofiber-networked bio-triboelectric generator: silk Bio-TEG. Adv Energy Mater. 2016;6(8):1502329. https://doi.org/10.1002/aenm.201502329.
12. Han Y, et al. Fish gelatin based triboelectric nanogenerator for harvesting biomechanical energy and self-powered sensing of human physiological signals. ACS Appl Mater Interfaces. 2020;12(14):16442–50. https://doi.org/10.1021/acsami.0c01061.
13. Jie Y, et al. Natural leaf made triboelectric nanogenerator for harvesting environmental mechanical energy. Adv Energy Mater. 2018;8(12):1703133. https://doi.org/10.1002/aenm.201703133.
14. Meder F, et al. Energy conversion at the cuticle of living plants. Adv Funct Mater. 2018;28(51):1806689. https://doi.org/10.1002/adfm.201806689.
15. Chen Y, et al. Triboelectrification on natural rose petal for harvesting environmental mechanical energy. Nano Energy. 2018;50:441–7. https://doi.org/10.1016/j.nanoen.2018.05.021.
16. Nandy S, et al. Cellulose: a contribution for the zero e-waste challenge. Adv Mater Technol. 2021. https://doi.org/10.1002/admt.202000994.
17. Yao C, Hernandez A, Yu Y, Cai Z, Wang X. Triboelectric nanogenerators and power-boards from cellulose nanofibrils and recycled materials. Nano Energy. 2016;30:103–8. https://doi.org/10.1016/j.nanoen.2016.09.036.
18. Peng J, et al. A composite generator film impregnated with cellulose nanocrystals for enhanced triboelectric performance. Nanoscale. 2016;9:1428–33. https://doi.org/10.1039/C6NR07602E.
19. Cui P, Parida K, Lin M-F, Xiong J, Cai G, Lee PS. Transparent, flexible cellulose nanofibril-phosphorene hybrid paper as triboelectric nanogenerator. Adv Mater Interfaces. 2017;4(22):1700651. https://doi.org/10.1002/admi.201700651.
20. Han J, et al. Paper-based triboelectric nanogenerators and their applications: a review. Beilstein J Nanotechnol. 2021;12:151–71. https://doi.org/10.3762/bjnano.12.12.
21. Jang S, Kim H, Oh JH. Simple and rapid fabrication of pencil-on-paper triboelectric nanogenerators with enhanced electrical performance. Nanoscale. 2017;9(35):13034–41. https://doi.org/10.1039/C7NR04610C.
22. He X, et al. An ultrathin paper-based self-powered system for portable electronics and wireless human-machine interaction. Nano Energy. 2017;39:328–36. https://doi.org/10.1016/j.nanoen.2017.06.046.
23. Xia K, Du C, Zhu Z, Wang R, Zhang H, Xu Z. Sliding-mode triboelectric nanogenerator based on paper and as a self-powered velocity and force sensor. Appl Mater Today. 2018;13:190–7. https://doi.org/10.1016/j.apmt.2018.09.005.
24. Yi F, et al. Stretchable-rubber-based triboelectric nanogenerator and its application as self-powered body motion sensors. Adv Funct Mater. 2015;25(24):3688–96. https://doi.org/10.1002/adfm.201500428.
25. Zhang S, et al. An all-rubber-based woven nanogenerator with improved triboelectric effect for highly efficient energy harvesting. Mater Lett. 2021;287:129271. https://doi.org/10.1016/j.matlet.2020.129271.
26. Bunriw W, Harnchana V, Chanthad C, Huynh VN. Natural rubber-TiO_2 nanocomposite film for triboelectric nanogenerator application. Polymers. 2021. https://doi.org/10.3390/polym13132213.
27. Suphasorn P, et al. Ag nanoparticle-incorporated natural rubber for mechanical energy harvesting application. Molecules. 2021. https://doi.org/10.3390/molecules26092720.
28. Natarajan TS, et al. Robust triboelectric generators by all-in-one commercial rubbers. ACS Appl Electron Mater. 2020;2(12):4054–64. https://doi.org/10.1021/acsaelm.0c00846.
29. Ren X, Fan H, Ma J, Wang C, Zhao Y, Lei S. Triboelectric nanogenerators based on fluorinated wasted rubber powder for self-powering application. ACS Sustainable Chem. Eng. 2017. https://doi.org/10.1021/acssuschemeng.6b02756.
30. Kim Y, Wu X, Oh JH. Fabrication of triboelectric nanogenerators based on electrospun polyimide nanofibers membrane. Sci Rep. 2020;10(1):2742. https://doi.org/10.1038/s41598-020-59546-7.
31. Li S, et al. Manipulating the triboelectric surface charge density of polymers by low-energy helium ion irradiation/implantation. Energy Environ Sci. 2020;13(3):896–907. https://doi.org/10.1039/C9EE03307F.
32. Zou H, et al. Quantifying the triboelectric series. Nat Commun. 2019;10(1):1427. https://doi.org/10.1038/s41467-019-09461-x.
33. Šutka A, Linarts A, Mālnieks K, Stiprais K, Lapčinskis L. Dramatic increase in polymer triboelectrification by transition from a glassy to rubbery state. Mater Horiz. 2020;7(2):520–3. https://doi.org/10.1039/C9MH01425J.
34. Sherrell PC, et al. Probing contact electrification: a cohesively sticky problem. ACS Appl Mater Interfaces. 2021;13(37):44935–47. https://doi.org/10.1021/acsami.1c13100.
35. Dharmasena RDIG, Deane JHB, Silva SRP. Nature of power generation and output optimization criteria for triboelectric nanogenerators. Adv Energy Mater. 2018;8(31):1802190. https://doi.org/10.1002/aenm.201802190.
36. Dudem B, et al. Exploring the theoretical and experimental optimization of high-performance triboelectric nanogenerators using micro-architectured silk cocoon films. Nano Energy. 2020;74:104882. https://doi.org/10.1016/j.nanoen.2020.104882.
37. Yang B, Zeng W, Peng Z, Liu S, Chen K, Tao X. A fully verified theoretical analysis of contact-mode triboelectric nanogenerators as a wearable power source. Adv Energy Mater. 2016;6(16):1600505. https://doi.org/10.1002/aenm.201600505.
38. Verners O, et al. Smooth polymers charge negatively: controlling contact electrification polarity in polymers. Nano Energy. 2022;104:107914. https://doi.org/10.1016/j.nanoen.2022.107914.
39. Šutka A, et al. The role of intermolecular forces in contact electrification on polymer surfaces and triboelectric nanogenerators. Energy Environ Sci. 2019;12(8):2417–21. https://doi.org/10.1039/C9EE01078E.

40. Byun K-E, et al. Control of triboelectrification by engineering surface dipole and surface electronic state. ACS Appl. Mater. Interfaces. 2016. https://doi.org/10.1021/acsami.6b02802.
41. Xu J, Zou Y, Nashalian A, Chen J. Leverage surface chemistry for high-performance triboelectric nanogenerators. Front Chem. 2020;8:577327. https://doi.org/10.3389/fchem.2020.577327.
42. Rolere S, Liengprayoon S, Vaysse L, Sainte-Beuve J, Bonfils F. Investigating natural rubber composition with Fourier Transform Infrared (FT-IR) spectroscopy: a rapid and non-destructive method to determine both protein and lipid contents simultaneously. Polym Testing. 2015;43:83–93. https://doi.org/10.1016/j.polymertesting.2015.02.011.
43. Cai X, Lei T, Sun D, Lin L. A critical analysis of the α, β and γ phases in poly(vinylidene fluoride) using FTIR. RSC Adv. 2017;7(25):15382–9. https://doi.org/10.1039/C7RA01267E.
44. Lin Y, et al. Studies on the electrostatic effects of stretched PVDF films and nanofibers. Nanoscale Res Lett. 2021;16(1):79. https://doi.org/10.1186/s11671-021-03536-9.
45. Zhu G, et al. A shape-adaptive thin-film-based approach for 50% high-efficiency energy generation through micro-grating sliding electrification. Adv Mater. 2014;26(23):3788–96. https://doi.org/10.1002/adma.201400021.
46. Niu S, et al. A theoretical study of grating structured triboelectric nanogenerators. Energy Environ Sci. 2014;7(7):2339–49. https://doi.org/10.1039/C4EE00498A.
47. Xie Y, et al. Grating-structured freestanding triboelectric-layer nanogenerator for harvesting mechanical energy at 85% total conversion efficiency. Adv Mater. 2014;26(38):6599–607. https://doi.org/10.1002/adma.201402428.
48. Zhang D, Shi J, Si Y, Li T. Multi-grating triboelectric nanogenerator for harvesting low-frequency ocean wave energy. Nano Energy. 2019;61:132–40. https://doi.org/10.1016/j.nanoen.2019.04.046.
49. Niu S, et al. Theoretical investigation and structural optimization of single-electrode triboelectric nanogenerators. Adv Funct Mater. 2014;24(22):3332–40. https://doi.org/10.1002/adfm.201303799.